Performance Analysis of Compact FD-MIMO Antenna Arrays in a Correlated Environment

Qurrat-Ul-Ain Nadeem, Abla Kammoun, Merouane Debbah, Mohamed-Slim Alouini

Performance Analysis of Compact FD-MIMO Antenna Arrays in a Correlated Environment

Qurrat-Ul-Ain Nadeem, *Student Member, IEEE,* Abla Kammoun, *Member, IEEE,*
Mérouane Debbah, *Fellow, IEEE,* and Mohamed-Slim Alouini, *Fellow, IEEE*

Abstract—**Full dimension multiple-input-multiple-output (FD-MIMO) is one of the key technologies proposed in the 3rd Generation Partnership Project (3GPP) for the fifth generation (5G) communication systems. The reason can be attributed to its ability to yield significant performance gains through the deployment of active antenna elements at the base station in the vertical as well as the conventional horizontal directions, enabling several elevation beamforming strategies. The resulting improvement in spectral efficiency largely depends on the orthogonality of the sub-channels constituting the FD-MIMO system. Accommodating a large number of antenna elements with sufficient spacing poses several constraints for practical implementation, making it imperative to consider compact antenna arrangements that minimize the overall channel correlation. Two such configurations considered in this work are the uniform linear array (ULA) and uniform circular array (UCA) of antenna ports, where each port is mapped to a group of physical antenna elements arranged in the vertical direction. The generalized analytical expression for the spatial correlation function (SCF) for the UCA is derived, exploiting results on spherical harmonics and Legendre polynomials. The mutual coupling between antenna dipoles is accounted for and the resulting SCF is also presented. The second part of this work compares the spatial correlation and mutual information (MI) performance of the ULA and UCA configurations in the 3GPP 3D urban-macro and urban-micro cell scenarios, utilizing results from Random Matrix Theory (RMT) on the deterministic equivalent of the MI for the Kronecker channel model. Simulation results study the performance patterns of the two arrays as a function of several channel and array parameters and identify applications and environments suitable for the deployment of each array.**

Index Terms—**Full-dimension (FD) multiple-input multiple-output (MIMO), spatial correlation, antenna arrays, massive MIMO, mutual information, mutual coupling.**

I. Introduction

Massive multiple-input multiple-output (MIMO) technology has received tremendous attention in the last decade primarily due to its ability to improve the spectral efficiency and user experience through the deployment of large-scale antenna arrays at the base station (BS), which exploit the multipath richness present in the spatial domain. However,

large spatial multiplexing gains can only be realized when the sub-channels constituted by the individual antennas in the array are uncorrelated. It is, therefore, important to develop a pragmatic perspective of MIMO communications in realistic propagation channels, where the presence of spatial correlation significantly deteriorates the system performance [1]–[3].

In order to be compatible with the existing 3rd Generation Partnership Project (3GPP) Long Term Evolution (LTE) standard, most commercial solutions consider the deployment of fewer than ten horizontally placed antennas at the BS [4]. An obvious way to achieve high performance in a correlated environment is to have a large separation between these antennas. However, accommodating a large number of antennas with sufficient spacing in the azimuth plane alone poses several constraints for practical implementation, given the BS form factor limitation. As a consequence, it is imperative to consider compact antenna array topologies that pack the antennas intelligently in the elevation as well as the traditional azimuth dimensions so as to minimize the overall channel correlation.

Most of the existing works in this area consider two-dimensional (2D) cellular layouts and investigate the spatial correlation in the azimuth plane only [5]–[8], without realizing that an explicit relationship exists between the correlation and the angular domain, which consists of both the azimuth and elevation dimensions. Due to the three-dimensional (3D) nature of real world transmission channels, beamforming in the azimuth alone can not fully exploit all the degrees of freedom offered by the channel. In fact, several possibilities have opened up in the recent years for the use of the elevation plane of the antenna radiation pattern for performance optimization through the deployment of active antenna elements in a 2D or 3D array panel [9]–[11]. This results in full dimension (FD) MIMO [12], [13], which has been identified as a promising technology for the next generation cellular systems in the 3GPP Release 12 and 13 workshops [14], [15]. Initial field trials have demonstrated the potential performance gain of this technology [10], [16] and standardization activity has been initiated in the 3GPP to develop 3D channel models and identify key areas in the existing LTE standards that need enhancement for the seamless integration of this technology into the current 4G LTE systems [15], [17].

The absence of elevation dimension is not the only limitation of the existing correlation models. These models have generally been derived in the literature for particular Angle of Departure (AoD)/ Angle of Arrival (AoA) distributions such as the uniform, Gaussian, cosine, Von Mises, Laplacian [5]–[8], [18]. The authors in [8] derived the correlation expressions

Q.-U.-A. Nadeem, A. Kammoun and M.-S. Alouini are with the Computer, Electrical, and Mathematical Sciences and Engineering (CEMSE) Division, King Abdullah University of Science and Technology (KAUST), Thuwal, Makkah Province, Saudi Arabia (e-mail: {qurratulain.nadeem,abla.kammoun,slim.alouini}@kaust.edu.sa)

M. Debbah is with Supélec, Gif-sur-Yvette, France and Mathematical and Algorithmic Sciences Lab, Huawei France R&D, Paris, France (e-mail: merouane.debbah@huawei.com, merouane.debbah@supelec.fr).

for the uniform circular array (UCA) and uniform linear array (ULA) configurations for Gaussian and uniform angular distributions, considering only azimuth angles and omnidirectional antennas. The proposed analysis relied on numerical integration methods to compute the correlation coefficients for the circular array for Gaussian angular distribution. The authors in [18] developed closed-form expressions for the spatial correlation for a compact antenna array under Gaussian AoA distribution assumption, taking into account the effects of mutual coupling (MC) between the antennas.

There are some works that consider spatial correlation in 3D propagation scenarios [19]–[25]. However, all these works consider passive omnidirectional antenna elements arranged in the azimuth plane only and the correlation analysis is done for only specific forms of underlying angular distributions. The authors in [23] demonstrated that the signal correlation between antenna elements of the UCA can be calculated directly from its spherical-wave coefficients for certain distributions of the azimuth and elevation AoAs. The authors in [21] used the spherical harmonic expansion (SHE) of plane waves to obtain analytical expressions for the spatial correlation for several angular distributions. The analysis is useful, but makes some assumptions on the nature of the underlying angular distributions, which do not accurately represent the attributes of real-world propagation scenarios.

The channel conditions and the choice of antenna array topology together determine the extent of performance gains realizable through the deployment of multiple antennas at the BS and the mobile station (MS). Most of the current research focuses on the impact of different channel conditions on the system performance [24], [25], without studying the impact of the choice of the antenna array topology. The problem becomes more acute in massive MIMO systems, where an even larger number of antenna elements needs to be packed in a limited space. Given the BS form factor limitation, the ULA of antenna ports, where each port is mapped to a group of physical antenna elements arranged in the vertical dimension, also referred to as the uniform rectangular array of antenna elements, has been proposed in the current 3GPP standards for deployment in FD massive MIMO settings [26]. The UCA of antenna ports can be another candidate antenna array topology for FD-MIMO implementation, which will allow for the compact arrangement of antenna elements in the 3D space.

There have not been many comprehensive studies to compare the performance of the ULA and UCA configurations, which can help in identifying the applications and radio environments suitable for their deployment. The authors in [19] studied some compact antenna array topologies by developing spatial correlation expressions under the uniform AoA distribution assumption. They analyzed the sensitivity of these arrays to several channel parameters and compared their mutual information (MI) performance. The authors in [27] compared the bit error rate performance of the ULA and UCA configurations in Rayleigh fading channels for a 2D channel model and truncated Gaussian azimuth AoA distribution. The numerical results were obtained for a very small number of antennas and showed that the UCA outperforms the ULA for moderate angular spreads and similar array sizes. The authors

in [20] derived spatial correlation expressions under the impact of MC for the ULA, UCA and uniform rectangular array configurations for uniform azimuth and elevation angular distributions. The MI analysis showed that the ULA performance is very sensitive to MC and spatial parameters.

In our study of FD-MIMO antenna array configurations, we make two main contributions. In the first part of this paper, we derive a generalized analytical expression for the spatial correlation function (SCF) for the UCA of antenna ports in a 3D cellular layout, where each antenna port is mapped to a group of physical antenna elements arranged in the vertical direction. The derivation exploits results on spherical harmonics and Legendre polynomials. The final expression depends on the angular parameters and the geometry of the array through the Fourier Series (FS) coefficients of the power spectra, and can be used to compute correlation coefficients for any arbitrary 3D propagation environment. The analysis follows the guidelines in [28], where the SCF for the ULA topology was worked out. However, the derivation for the UCA is more involved owing to the more intricate nature of the array response vector. The expression for the spatial correlation taking into account the mutual coupling (MC) effects between the antenna dipoles is also derived.

The second part of this paper thoroughly compares the spatial correlation performance of the ULA and UCA configurations. The SCF for the UCA derived here and the SCF for the ULA presented in [28] are used to determine the theoretical covariance matrices at the transmitter and the receiver and form the Kronecker channel model. The MI performance of the two arrays is then evaluated by utilizing the information-theoretic deterministic equivalent of the MI developed for the Kronecker channel model in [29] using results from Random Matrix Theory (RMT). The performance patterns of the two arrays are compared in the 3D urban-macro (UMa) and 3D urban-micro (UMi) scenarios proposed in the 3GPP and WINNER+ standards [17], [30], as a function of several channel and array parameters, including mean azimuth and elevation AoD/AoA, angular spreads, the number of antennas and antenna spacing. Some useful insights into the impact of MC on the spatial correlation and MI performance of the two arrays are also provided. Results show that for equal array sizes, the ULA outperforms the UCA for high angular spreads and low number of antennas to array width ratio, making it a suitable candidate for rich scattering environments. However, UCA is a more appropriate choice in massive MIMO settings, where the circular arrangement of antenna ports will minimize the overall correlation experienced by a large number of antennas arranged in a confined space. We believe that the conclusions drawn will assist in the identification of appropriate deployment scenarios for the two arrays.

The rest of the paper is organized as follows. Section II describes the UCA configuration and the corresponding 3D channel model. The analytical expressions for the SCF with and without accounting for the MC effects are derived in section III. Section IV compares the spatial correlation and MI performance of the ULA and the UCA topologies as a function of several channel and array parameters using numerical results. Finally, section V concludes the paper.
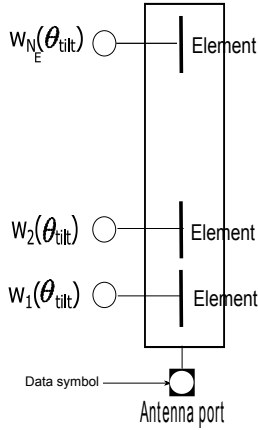
Fig. 1: Antenna port structure.

Fig. 2: UCA of antenna ports.

II. ANTENNA ARRAY CONFIGURATION AND 3D CHANNEL MODEL

The key source of performance enhancement in FD-MIMO systems is the deployment of active antenna elements in both the horizontal and vertical directions, wherein adaptive and dynamic precoding can be performed jointly across all elements to help realize different 3D beamforming scenarios. The traditional spatial channel model (SCM) used in theoretical researches and wireless communication standards is a 2D channel model which ignores the elevation angles of the signal paths and is utilized for the evaluation of technologies designed for BSs equipped with horizontally placed antenna elements. However, for the evaluation and design of FD-MIMO, such 2D channel models are not adequate and 3D SCMs need to be developed. This section introduces the antenna configuration based on the circular arrangement of antenna ports and outlines a simplified 3D SCM which is inspired from the ongoing standardization efforts in the 3GPP, but is more tractable for the correlation analysis later.

A. Antenna Configuration

To help readers understand the use of elevation beamforming techniques in practice, we will introduce the antenna configuration and radiation pattern expressions being proposed in the current standardization works. In LTE, the radio resource is organized on the basis of antenna ports, also referred to as transceiver units or columns [15], [26]. Each antenna port is mapped to N_E physical antenna elements arranged along the vertical direction. The 3D beamforming techniques aim at realizing spatially separated transmission links to a large number of MSs. One possible way to do this is to build antenna ports that transmit narrow vertical beams at different downtilt angles, where the downtilt angle achieved by a port is denoted by θ_{tilt}. The N_E antenna elements constituting a port are fed with the same signal with corresponding weights $w_k(\theta_{tilt})$, $k = 1, \ldots N_E$, to focus the transmitted wavefront in the direction of the targeted MS [10], [17], [31]. The higher is the value of N_E, the narrower is the beam that can be transmitted from a port. The structure of a typical antenna port is shown in Fig. 1 [17], [31]. Several such antenna ports
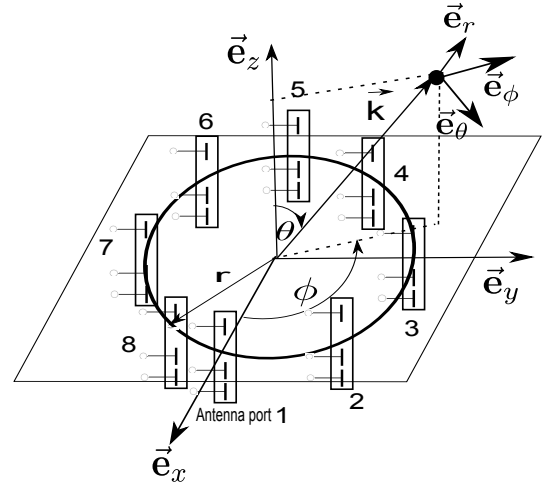
can be used, where every port can be fed with a different signal intended for a different user. At the MS, each antenna port appears as a single antenna, because its elements carry the same signal. We are therefore interested in the channel between the transmitting antenna port and the receiver side instead of the channel between the individual elements.

In this work we focus on the UCA configuration shown in Fig. 2, where the antenna ports are arranged in a circle of radius r in the $(\hat{\mathbf{e}}_x, \hat{\mathbf{e}}_y)$ plane, with the reference point at the center of the circle. Every port is mapped to N_E physical antenna elements arranged along the $\hat{\mathbf{e}}_z$ direction.

In theory, the antenna port pattern depends on the number of antenna elements constituting the port, their patterns, relative positions and corresponding weights. Antenna elements are usually manufactured with a fixed beamwidth, and antenna manufacturers typically offer a limited number of beamwidth variations within their conventional product lines. Organizing these elements into ports provides control over the half power beamwidth (HPBW) and maximum gain of the overall antenna port. The values of important antenna element parameters based on the 3GPP standards are provided in Table 1 [17], [26]. The subscript 'E' is to stress on the fact that these values are for antenna elements. For the values of N_E and inter-element separation specified in Table 1, the gain and HPBW of the overall antenna port can be calculated using a simple relationship in [32]. The parameter values for the antenna port are provided in Table 2 [33], [34].

To enable an abstraction of the role played by the antenna elements to perform the downtilt, ITU channel model approximates the vertical radiation pattern of each port by a narrow

TABLE I: Antenna element parameters.

Parameter	Value
Carrier Frequency	2GHz
N_E, Inter-element separation	10, 0.5 λ
Azimuth HPBW $\phi_{3dB,E}$	65°
Elevation HPBW $\theta_{3dB,E}$	65°
Maximum directional element gain $G_{E,max}$	8dBi
Side-lobe attenuation $SLA_{v,E}$	30dB
Maximum attenuation $A_{m,E}$	30dB.

beam in the elevation plane with HPBW, $\theta_{3dB} = 15^o$. We take this 'antenna port approach' and model the channel between antenna ports instead of antenna elements. The combined antenna port radiation pattern is given in dB as follows [33], [34], [31],

$$A_p(\phi, \theta, \theta_{tilt}) = G_{p,max} - \min\{-(A_H(\phi) + A_V(\theta, \theta_{tilt})), A_m\}$$
(1)

where,

$$A_H(\phi) = -\min\left[12\left(\frac{\phi}{\phi_{3dB}}\right)^2, A_m\right],$$

$$A_V(\theta, \theta_{tilt}) = -\min\left[12\left(\frac{\theta - \theta_{tilt}}{\theta_{3dB}}\right)^2, A_m\right], \quad (2)$$

where $A_H(\phi)$ and $A_V(\theta, \theta_{tilt})$ are the horizontal and vertical antenna patterns, ϕ and θ represent the azimuth and the elevation AoDs respectively and θ_{tilt} is the electrical tilt angle. A_m is defined in Table 2. For an antenna port with vertically polarized antenna elements, the global field pattern along the horizontal polarization is zero and along the vertical polarization is given by $\sqrt{A_p(\phi, \theta, \theta_{tilt})|_{lin}}$ [[34], Section A.2.1.6.1, p. 79]. Denoting $A_p(\phi, \theta, \theta_{tilt})|_{lin}$ as $10^{\frac{G_{p,max}}{10}} g_t(\phi, \theta, \theta_{tilt})$, the field pattern along the vertical polarization in linear scale can be decomposed as $g_t(\phi, \theta, \theta_{tilt}) \approx g_{t,H}(\phi) g_{t,V}(\theta, \theta_{tilt})$, with the horizontal and vertical field patterns given by,

$$g_{t,H}(\phi) = \exp\left(-1.2\left(\frac{\phi}{\phi_{3dB}}\right)^2 \ln 10\right), \quad (3)$$

$$g_{t,V}(\theta, \theta_{tilt}) = \exp\left(-1.2\left(\frac{\theta - \theta_{tilt}}{\theta_{3dB}}\right)^2 \ln 10\right). \quad (4)$$

B. 3D Channel Model

The SCM used for the evaluation of different standardized technologies operating with BSs equipped with horizontally placed antenna elements is a 2D channel model, developed and refined over the years by a number of research and standardization efforts in the 3GPP community. This 2D model ignores the modeling of the elevation angles of the propagation paths for simplicity, even though the propagation environments are 3D in nature. However, when evaluating the performance of FD-MIMO systems, which consider the arrangement of antenna elements in both the azimuth and elevation planes, it is important for channel models to account for the elevation angles of the propagation paths and also capture the directional antenna radiation pattern in the vertical direction.

Encouraged by the preliminary results on the potential of elevation beamforming to enhance the system performance, the 3GPP has recently completed a thorough study on the

TABLE II: Antenna port parameters.

Parameter	Value
Carrier Frequency	2GHz
Azimuth HPBW ϕ_{3dB}	65°
Elevation HPBW θ_{3dB}	15°
Maximum directional port gain $G_{p,max}$	17dBi
Maximum attenuation A_m	20dB.

3D channel model in [17]. Like its 2D counterparts, this channel model also follows a system-level approach, wherein channel realizations are generated by summing contributions of N propagation paths, also referred to as clusters. Every cluster is characterized by its time delay, AoD (ϕ_n, θ_n) and AoA (φ_n, ϑ_n), where ϕ_n and θ_n correspond to the azimuth and elevation AoD of the nth cluster respectively, and φ_n and ϑ_n correspond to the azimuth and elevation AoA of the nth cluster respectively. Additionally, the standardized channel models assume that every cluster gives rise to M unresolvable subpaths which have the same delay and mean AoD/AoA as the overall cluster [31]. The clusters are described through large scale parameters such as the delay spread, shadow fading and azimuth and elevation angular spreads. These parameters are drawn from given distributions and serve to generate the cluster powers, delays and angles, often referred to as small scale parameters.

The channel model used in this work is inspired from the 3GPP 3D channel model in [17], but makes some realistic assumptions on the channel parameters to make the model tractable for the subsequent theoretical analysis in this work. In particular, the assumption made in the standards that every cluster gives rise to M unresolvable subpaths has been dropped. Since these subpaths are assumed to be unresolvable in the standards and are centered around the AoD/AoA of the original cluster, so their spatial properties are quite similar and are well-captured by the spatial parameters defined for the overall cluster. The channel realizations are therefore generated by summing the contributions of N clusters. Based on this discussion, the narrowband 3D channel between the BS antenna port s and the MS antenna port u is given by [17], [31],

$$[\mathbf{H}]_{su} = \sqrt{10^{-(PL+\sigma_{SF}-G_{p,max})/10}} \sum_{n=1}^{N} \alpha_n \sqrt{g_t(\phi_n, \theta_n, \theta_{tilt})}$$

$$\times \sqrt{g_r(\varphi_n, \vartheta_n)} [\mathbf{a}_r(\varphi_n, \vartheta_n)]_u [\mathbf{a}_t(\phi_n, \theta_n)]_s, \quad (5)$$

where PL and σ_{SF} are used to denote the loss incurred by path loss and shadow fading respectively in dB, and $\alpha_n \sim \mathcal{CN}(0, \frac{1}{N})$ is the complex amplitude of the nth cluster. For vertically polarized elements, $\sqrt{g_t(\phi_n, \theta_n, \theta_{tilt})}$ and $\sqrt{g_r(\varphi_n, \vartheta_n)}$ are the global field patterns of the BS antenna port and MS antenna port respectively. Also, $\mathbf{a}_t(\phi, \theta)$ and $\mathbf{a}_r(\varphi, \vartheta)$ are the array response vectors of the antennas at the BS and the MS respectively with entries given by,

$$[\mathbf{a}_t(\phi, \theta)]_s = \exp(i\mathbf{k}_t.\mathbf{x}_s), \quad (6)$$

$$[\mathbf{a}_r(\varphi, \vartheta)]_u = \exp(i\mathbf{k}_r.\mathbf{x}_u), \quad (7)$$

where . is the scalar product, i is the imaginary unit, $\mathbf{x}_s$ is the location vector of the sth transmit (Tx) antenna port, $\mathbf{x}_u$ is the location vector of the uth receive (Rx) antenna port, and $\mathbf{k}_t$ and $\mathbf{k}_r$ are the Tx and Rx wave vectors respectively, where $\mathbf{k} = k\hat{\mathbf{v}}$, with $k = \frac{2\pi}{\lambda}$. Note that λ is the wavelength of the carrier and $\hat{\mathbf{v}}$ represents the unit vector in direction of wave propagation.

Given the UCA configuration of radius r in Fig. 2 with N_{BS} Tx antenna ports and N_{MS} Rx antenna ports, $[\hat{\mathbf{v}}_t.\mathbf{x}_s] =$

$r\cos(\phi - \psi_s)\sin\theta$, where $\psi_s = \frac{2\pi(s-1)}{N_{BS}}, s = 1, \ldots, N_{BS}$, and $[\hat{\mathbf{v}}_r.\mathbf{x}_u] = r\cos(\varphi - \upsilon_u)\sin\vartheta$, where $\upsilon_u = \frac{2\pi(u-1)}{N_{MS}}, u = 1, \ldots, N_{MS}$. The 3D channel between the sth Tx antenna port and the uth Rx antenna port in (5) can therefore be written as,

$$[\mathbf{H}]_{su} = \sqrt{10^{-(PL+\sigma_{SF}-G_{p,max})/10}} \sum_{n=1}^{N} \alpha_n \sqrt{g_t(\phi_n, \theta_n, \theta_{tilt})}$$
$$\times \sqrt{g_r(\varphi_n, \vartheta_n)} \exp\left(ikr\cos(\phi_n - \psi_s)\sin\theta_n\right)\exp(ikr \quad (8)$$
$$\times \cos(\varphi_n - \upsilon_u)\sin\vartheta_n), \quad s = 1, \ldots, N_{BS}, \ u = 1, \ldots, N_{MS}.$$

III. SPATIAL CORRELATION FUNCTION FOR A UNIFORM CIRCULAR ARRAY

Compact structure of large-scale antenna arrays and low values of elevation angular spread in realistic propagation environments drastically increase the spatial correlation in FD-MIMO systems. It is therefore imperative to characterize and take this correlation into account to allow for an accurate performance evaluation of FD-MIMO techniques. In this section, we derive a generalized analytical expression for the SCF for the 3D MIMO channel constituted by the UCAs of antenna ports at the BS and the MS. The final expression will be shown to depend on the FS coefficients of the power azimuth spectrum (PAS) and the power elevation spectrum (PES) of the propagation scenario under investigation. We will first elaborate on the concepts of PAS and PES, before proceeding to the derivation of the SCF.

A. Power Spectra

Power azimuth and elevation spectra are important statistical properties of wireless channels, that influence the spatial correlation present in MIMO systems [35]. PAS describes the spatial distribution of the expected power in the azimuth dimension, while PES describes the distribution in the elevation. They are expressed using the 3D antenna radiation pattern and the azimuth and elevation angular power density functions of the radio waves. For the spherical coordinate system $(\hat{\mathbf{e}}_r, \hat{\mathbf{e}}_\theta, \hat{\mathbf{e}}_\phi)$ shown in Fig. 2, the joint angular power density function $p(\phi, \theta)$ is related to the joint angular probability distribution function $f(\phi, \theta)$ by [36],

$$p(\phi, \theta) = \frac{f(\phi, \theta)}{\sin(\theta)}. \quad (9)$$

Obtaining the marginal probability distribution for θ yields the relationship between the elevation power density function $p_\theta(\theta)$, and the elevation probability distribution function $f_\theta(\theta)$ as,

$$p_\theta(\theta) = \frac{f_\theta(\theta)}{\sin(\theta)}. \quad (10)$$

Observing that the integral of the product of the Tx antenna port radiation pattern and the angular power density function gives the expected power transmitted by an antenna port, we define the PAS and the PES at the transmitter respectively as,

$$\text{PAS}_t(\phi) = g_{t,H}(\phi)p_\phi(\phi), \quad (11)$$

where $p_\phi(\phi)$ is the azimuth power density function which equals the azimuth probability density function $f_\phi(\phi)$ and,

$$\text{PES}_t(\theta, \theta_{tilt}) = g_{t,V}(\theta, \theta_{tilt})p_\theta(\theta). \quad (12)$$

The expressions for PAS_r and PES_r can be obtained similarly.

B. Analytical Expression for the SCF

The analysis in this section will leverage the mathematical convenience of the SHE of plane waves and the properties of Legendre and associated Legendre polynomials, provided in Appendix A. It can be seen from (8) that for $\alpha_n \sim i.i.d$ $\mathcal{CN}(0, \frac{1}{N})$, the SCF for the channels constituted by any pair of Tx antenna ports and Rx antenna ports can be expressed as,

$$\text{SCF}_{\text{uca}} = \mathbb{E}[[\mathbf{H}]_{su}[\mathbf{H}_{s'u'}^H]]$$
$$= 10^{-(PL+\sigma_{SF}-G_{p,max})/10}\rho_t(s, s')\rho_r(u, u'), \quad (13)$$

where,

$$\rho_t(s, s') = \mathbb{E}\left[g_t(\phi, \theta, \theta_{tilt})\exp\left(i\frac{2\pi}{\lambda}r\sin\theta(\cos(\phi - \psi_s)\right.\right.$$
$$\left.\left. - \cos(\phi - \psi_{s'}))\right)\right], \quad (14)$$
$$\rho_r(u, u') = \mathbb{E}\left[g_r(\varphi, \vartheta)\exp\left(i\frac{2\pi}{\lambda}r\sin\vartheta(\cos(\varphi - \upsilon_u)\right.\right.$$
$$\left.\left. - \cos(\varphi - \upsilon_{u'}))\right)\right], \quad (15)$$

where $\psi_s = \frac{2\pi(s-1)}{N_{BS}}, \psi_{s'} = \frac{2\pi(s'-1)}{N_{BS}}$ and $\upsilon_u = \frac{2\pi(u-1)}{N_{MS}}, \upsilon_{u'} = \frac{2\pi(u'-1)}{N_{MS}}$, where $s, s' = 1, \ldots, N_{BS}$ and $u, u' = 1, \ldots, N_{MS}$.

To facilitate the derivation, the expressions in (14) and (15) will be reformulated to give them a form similar to that of a plane electromagnetic wave, which can be expanded using the SHE result provided in Appendix A. The necessary steps are shown for (14). A closed-form expression for (15) can be obtained similarly.

Defining $Z_1 = \cos\psi_s - \cos\psi_{s'}$ and $Z_2 = \sin\psi_s - \sin\psi_{s'}$, $\rho_t(s, s')$ can be written as,

$$\rho_t(s, s') = \mathbb{E}\left[g_t(\phi, \theta, \theta_{tilt})\exp\left(i\frac{2\pi}{\lambda}r\sin\theta(Z_1\cos\phi\right.\right.$$
$$\left.\left. + Z_2\sin\phi)\right)\right]. \quad (16)$$

Next we define $c = \sqrt{Z_1^2 + Z_2^2}$ and

$$\zeta = \begin{cases} 0, & \text{if } Z_1 = 0 \ \& \ Z_2 = 0, \\ \arctan\left(\frac{Z_2}{Z_1}\right), & \text{if } Z_1 \geq 0 \ \& \ Z_2 > 0, \\ \pi + \arctan\left(\frac{Z_2}{Z_1}\right), & \text{if } Z_1 < 0 \ \& \ Z_2 \geq 0. \end{cases} \quad (17)$$

With these definitions, (16) can be reformulated as,

$$\rho_t(s, s') = \mathbb{E}\left[g_t(\phi, \theta, \theta_{tilt})\exp\left(i\frac{2\pi}{\lambda}rc\sin\theta\cos(\phi - \zeta)\right)\right], \quad (18)$$

for $(Z_1 = 0 \ \& \ Z_2 = 0)$, $(Z_1 \geq 0 \ \& \ Z_2 > 0)$ and $(Z_1 < 0 \ \& \ Z_2 \geq 0)$. Note that the other terms can be calculated as $\rho_t(s, s')$ for $(Z_1 \leq 0 \ \& \ Z_2 < 0) = \rho_t(s, s')^*$ for $(Z_1 \geq 0 \ \& \ Z_2 > 0)$ and $\rho_t(s, s')$ for $(Z_1 > 0 \ \& \ Z_2 \leq 0) = \rho_t(s, s')^*$ for $(Z_1 < 0 \ \& \ Z_2 \geq 0)$.

$$\rho_t(s,s') = \mathbb{E}[g_t(\phi,\theta,\theta_{tilt})]j_0\left(\frac{2\pi}{\lambda}rc\right) + \sum_{n=1}^{\infty}(-1)^n(4n+1)j_{2n}\left(\frac{2\pi}{\lambda}rc\right)P_{2n}(0)\mathbb{E}[P_{2n}(\cos\theta)g_{t,V}(\theta,\theta_{tilt})]\mathbb{E}[g_{t,H}(\phi)] + \sum_{n=1}^{\infty}4(-1)^n$$

$$\times\, j_{2n}\left(\frac{2\pi}{\lambda}rc\right)\left(\sum_{m=1}^{n}\bar{P}_{2n}^{2m}(0)\mathbb{E}[\bar{P}_{2n}^{2m}(\cos\theta)g_{t,V}(\theta,\theta_{tilt})]\Big(\cos(2m\zeta)\mathbb{E}[\cos(2m\phi)g_{t,H}(\phi)] + \sin(2m\zeta)\mathbb{E}[\sin(2m\phi)g_{t,H}(\phi)]\Big)\right)$$

$$-\sum_{n=1}^{\infty}4i(-1)^n j_{2n-1}\left(\frac{2\pi}{\lambda}rc\right)\left(\sum_{m=1}^{n}\bar{P}_{2n-1}^{2m-1}(0)\mathbb{E}[\bar{P}_{2n-1}^{2m-1}(\cos\theta)g_{t,V}(\theta,\theta_{tilt})]\Big(\cos((2m-1)\zeta)\mathbb{E}[\cos((2m-1)\phi)g_{t,H}(\phi)]\right.$$

$$\left. +\, \sin((2m-1)\zeta)\mathbb{E}[\sin((2m-1)\phi)g_{t,H}(\phi)]\Big)\right), \tag{21}$$

The SHE result for plane electromagnetic waves given in equation (40) in Appendix A is now exploited to yield an alternate expression for the exponential term in (18) as,

$$\exp\left(i\frac{2\pi}{\lambda}rc\sin\theta\cos(\phi-\zeta)\right) = \sum_{n=0}^{\infty}i^n(2n+1)j_n\left(\frac{2\pi}{\lambda}rc\right)$$
$$\times P_n(\sin\theta\cos(\phi-\zeta)). \tag{19}$$

Note that $\sin\theta\cos(\phi-\zeta)$ is the dot product of the unit wave vector $\hat{\mathbf{v}}$ with spherical coordinates (ϕ,θ), and $\hat{\mathbf{x}}$, the unit vector between the positions of sth and s'^{th} Tx antenna ports, with spherical coordinates $(\zeta,\frac{\pi}{2})$. Combining the addition theorem for Legendre polynomials given in Appendix A (41) with (19), and using the resulting expression in (18) would expand $\rho_t(s,s')$ as,

$$\rho_t(s,s') = \mathbb{E}\Big[g_t(\phi,\theta,\theta_{tilt})\sum_{n=0}^{\infty}i^n(2n+1)j_n\left(\frac{2\pi}{\lambda}rc\right)$$
$$\times\Big(P_n(\cos\theta)P_n(0) + 2\sum_{m=1}^{n}\frac{(n-m)!}{(n+m)!}P_n^m(\cos\theta)$$
$$\times P_n^m(0)\cos(m(\phi-\zeta))\Big)\Big]. \tag{20}$$

The properties of Legendre and associated Legendre polynomials provided in Appendix A along with some trigonometric manipulations are now exploited to obtain the following Lemma.

Lemma 1. For a uniform circular array of antenna ports with arbitrary antenna patterns and for arbitrary angular distributions, where $\phi \in [-\pi,\pi]$ and $\theta \in [0,\pi]$, the correlation between the channels constituted by any pair of Tx antennas ports can be expressed as (21), where $\bar{P}_n^m(x)=\sqrt{(n+\frac{1}{2})\frac{(n-m)!}{(n+m)!}}P_n^m(x)$ and $s,s'=1,\dots,N_{BS}$.

The expansion in (21) reveals several problems in deriving an analytical expression for the SCF. The random variables pertaining to the azimuth and elevation angles appear as arguments of Legendre polynomials, posing a challenge to the computation of the expectation terms in a closed-form. However, the use of the trigonometric expansions of Legendre and associated Legendre polynomials provided in Appendix A can produce an interesting analytical expression for $\rho_t(s,s')$. These expansions will help express the expectation terms in (21) as a linear combination of the scaled FS coefficients of the PAS and PES. After expanding the expectation terms in (21) using (43) from Appendix A, the generalized analytical

expression for the SCF for channels constituted by the (BS, MS) antenna port pairs (s,u) and (s',u') can be obtained and is presented in **Theorem 1** .

Theorem 1. For a UCA of antennas ports with arbitrary antenna patterns and for arbitrary angular distributions, where $\phi \in [-\pi,\pi]$ and $\theta \in [0,\pi]$, the SCF for the FD channels constituted by the (BS, MS) antenna port pairs (s,u) and (s',u') is given by,

$$\text{SCF}_{\text{uca}} = 10^{-(PL+\sigma_{SF}-G_{p,max})/10}\rho_t(s,s')\rho_r(u,u'), \tag{22}$$

where $\rho_t(s,s')$ and $\rho_r(u,u')$ are given by equations (23) and (24) respectively, for $(Z_1 = 0\ \&\ Z_2 = 0)$, $(Z_1 \geq 0\ \&\ Z_2 > 0)$ and $(Z_1 < 0\ \&\ Z_2 \geq 0)$, $s,s' = 1,\dots,N_{BS}$, $u,u' = 1,\dots,N_{MS}$, where $a_\phi(m), b_\phi(m), a_\theta(k)$ and $b_\theta(k)$ are the FS coefficients of the power spectra defined as,

$$a_\phi(m) = \frac{1}{\pi}\int_{-\pi}^{\pi}\text{PAS}_t(\phi)\cos(m\phi)d\phi, \tag{25}$$

$$b_\phi(m) = \frac{1}{\pi}\int_{-\pi}^{\pi}\text{PAS}_t(\phi)\sin(m\phi)d\phi, \tag{26}$$

$$a_\theta(k) = \frac{1}{\pi}\int_{0}^{2\pi}\text{PES}_t(\theta,\theta_{tilt})\cos(k\theta)d\theta, \tag{27}$$

$$b_\theta(k) = \frac{1}{\pi}\int_{0}^{2\pi}\text{PES}_t(\theta,\theta_{tilt})\sin(k\theta)d\theta. \tag{28}$$

Note that the other terms can be calculated as $\rho_t(s,s')$ for $(Z_1 \leq 0\ \&\ Z_2 < 0) = \rho_t(s,s')^*$ for $(Z_1 \geq 0\ \&\ Z_2 > 0)$ and $\rho_t(s,s')$ for $(Z_1 > 0\ \&\ Z_2 \leq 0) = \rho_t(s,s')^*$ for $(Z_1 < 0\ \&\ Z_2 \geq 0)$.

The proof of **Theorem 1** is provided in Appendix B. The theorem enables the computation of the correlation values for the 3D MIMO channel constituted by the UCAs of antenna ports at the BS and the MS for arbitrary choices of antenna patterns and angular distributions. It is possible to truncate the summations over n in **Theorem 1** to a small number, N_0, resulting in a bound on the truncation error that decreases exponentially with N_0 [37]. Using the analysis provided in *Remark 1* in [28], 18 terms are sufficient to bound the error in the correlation between adjacent antenna ports by approximately 0.5% for a UCA of 8 ports arranged in a radius of 2λ. The industrials and theoretical researchers interested in using this SCF need to provide only the Fourier Series (FS) coefficients of the power azimuth spectrum (PAS) and the power elevation spectrum (PES) for the propagation scenario under study.

$$\rho_t(s, s') = \pi^2 a_\phi(0) b_\theta(1) j_0\left(\frac{2\pi}{\lambda}rc\right) + \sum_{n=1}^{\infty}(-1)^n(4n+1)j_{2n}\left(\frac{2\pi}{\lambda}rc\right)P_{2n}(0)a_\phi(0)\pi^2\sum_{k=-n}^{n}p_{n-k}p_{n+k}$$

$$\times \frac{1}{2}[b_\theta(2k+1) - b_\theta(2k-1)] + \sum_{n=1}^{\infty}4(-1)^n j_{2n}\left(\frac{2\pi}{\lambda}rc\right)\left(\sum_{m=1}^{n}\bar{P}_{2n}^{2m}(0)\pi^2\sum_{k=0}^{n}c_{2n,2k}^{2m}\frac{1}{2}[b_\theta(2k+1)\right.$$

$$- b_\theta(2k-1)]\left(\cos(2m\zeta)a_\phi(2m) + \sin(2m\zeta)b_\phi(2m))\right) - \sum_{n=1}^{\infty}4i(-1)^n j_{2n-1}\left(\frac{2\pi}{\lambda}rc\right)\left(\sum_{m=1}^{n}\bar{P}_{2n-1}^{2m-1}(0)\pi^2\right.$$

$$\times \left(\cos((2m-1)\zeta)a_\phi(2m-1) + \sin((2m-1)\zeta)b_\phi(2m-1))\sum_{k=1}^{n}d_{2n-1,2k-1}^{2m-1}\frac{1}{2}[a_\theta(2k-2) - a_\theta(2k)]\right), \qquad (23)$$

$$\rho_r(u, u') = \pi^2 a_\varphi(0) b_\vartheta(1) j_0\left(\frac{2\pi}{\lambda}rc\right) + \sum_{n=1}^{\infty}(-1)^n(4n+1)j_{2n}\left(\frac{2\pi}{\lambda}rc\right)P_{2n}(0)a_\varphi(0)\pi^2\sum_{k=-n}^{n}p_{n-k}p_{n+k}$$

$$\times \frac{1}{2}[b_\vartheta(2k+1) - b_\vartheta(2k-1)] + \sum_{n=1}^{\infty}4(-1)^n j_{2n}\left(\frac{2\pi}{\lambda}rc\right)\left(\sum_{m=1}^{n}\bar{P}_{2n}^{2m}(0)\pi^2\sum_{k=0}^{n}c_{2n,2k}^{2m}\frac{1}{2}[b_\vartheta(2k+1)\right.$$

$$- b_\vartheta(2k-1)]\left(\cos(2m\zeta)a_\varphi(2m) + \sin(2m\zeta)b_\varphi(2m))\right) - \sum_{n=1}^{\infty}4i(-1)^n j_{2n-1}\left(\frac{2\pi}{\lambda}rc\right)\left(\sum_{m=1}^{n}\bar{P}_{2n-1}^{2m-1}(0)\pi^2\right.$$

$$\times \left(\cos((2m-1)\zeta)a_\varphi(2m-1) + \sin((2m-1)\zeta)b_\varphi(2m-1))\sum_{k=1}^{n}d_{2n-1,2k-1}^{2m-1}\frac{1}{2}[a_\vartheta(2k-2) - a_\vartheta(2k)]\right), \qquad (24)$$

C. Spatial Correlation with Mutual Coupling

A radio wave, when incident on an antenna element, induces an electric current in it. When several antenna elements are placed close to each other, the electromagnetic field generated by this induced current in one element alters the current distribution of the other elements causing mutual coupling (MC) between them. As a result, the gain, radiation pattern, and input impedance of each element is affected. Several works [18], [20], [38]–[40] have shown that this MC effect is non-negligible due to the spatial constraints at the BS and the miniaturization trend in mobile terminals.

Generally, it is assumed that MC is detrimental to the system performance in that it will increase the channel correlation and deteriorate the system capacity [41]. Recent investigations have come up with this interesting revelation that MC can in fact have a decorrelating effect on the channel coefficients. This favorable result is explained by the fact that MC causes pattern distortion and provides some form of pattern diversity [21], [40]. Under small antenna spacing, as is the case in compact antenna arrays, this pattern diversity effect dominates over the effect of the loss in spatial diversity resulting in lower correlation and higher capacity values [18], [20], [38]. However, these works have neglected the impact of the loss in the antenna gain and transmitted power that is incurred when MC is taken into account. This loss has been observed in [39], [40]. In this section, we will derive expressions for the spatial correlation under the effects of MC and use them in the subsequent sections to study the impact of MC on the channel correlation and MI.

The derivation of the SCF under MC effects will exploit results on the mutual impedance between antenna dipoles/elements, which have been developed in antenna the-

ory [32]. Since the grouping of these dipoles into ports is a rather new concept, so the mutual impedance expressions for antenna ports have not yet been developed. Consequently, in this section we will focus on N_{BS} antenna elements arranged in the UCA topology, instead of N_{BS} antenna ports.

To calculate the spatial correlation coefficients between the Tx antennas elements subject to MC, it is important to establish the relationship between the channels constituted by these elements with and without taking into account the MC effects. This relationship is given by [6], [18],

$$\mathbf{v} = \mathbf{Z}^{-1}\mathbf{s}, \qquad (29)$$

where $\mathbf{Z}$ is the mutual impedance matrix given by,

$$\mathbf{Z} = \begin{bmatrix} 1 + \frac{Z_{11}}{Z_L} & \frac{Z_{12}}{Z_L} & \cdots & \frac{Z_{1N_{BS}}}{Z_L} \\ \frac{Z_{21}}{Z_L} & 1 + \frac{Z_{22}}{Z_L} & \cdots & \frac{Z_{2N_{BS}}}{Z_L} \\ \vdots & \vdots & \ddots & \vdots \\ \frac{Z_{N_{BS}1}}{Z_L} & \frac{Z_{N_{BS}2}}{Z_L} & \cdots & 1 + \frac{Z_{N_{BS}N_{BS}}}{Z_L} \end{bmatrix}, \qquad (30)$$

where $Z_{ss'}$ is the self impedance of the antenna dipole if $s = s'$ and the mutual impedance between the sth and s'^{th} antenna dipoles if $s \neq s'$ with entries given by [32],

$$Z_{ss'} = \begin{cases} 30(0.577 + ln(2\pi) - Ci(2\pi) + iSi(2\pi)), \ s = s', \\ 30[2Ci(kd_{ss'}) - Ci(k\mu_{ss',1}) - Ci(k\mu_{ss',2})] - 30i \\ \times[2Si(kd_{ss'}) - Si(k\mu_{ss',1}) - Si(k\mu_{ss',2})], \ s \neq s', \end{cases}$$

where $k = \frac{2\pi}{\lambda}$, $\mu_{ss',1} = \sqrt{d_{ss'}^2 + l^2} + l$ and $\mu_{ss',2} = \sqrt{d_{ss'}^2 + l^2} - l$, l is the dipole length, $d_{ss'}$ is the distance between elements s and s' and $Ci(x)$ and $Si(x)$ are the integral cosine and sine functions respectively. Note that the self-impedance expression is given for the typical dipole length

value of $\lambda/2$. For the UCA topology, the vector of channel responses at the Tx side without accounting for the MC effects is given by,

$$
\mathbf{s} = \begin{bmatrix} \sqrt{g_t(\phi,\theta,\theta_{tilt})} \exp\left(ikr\cos(\phi-\psi_1)\sin\theta\right) \\ \sqrt{g_t(\phi,\theta,\theta_{tilt})} \exp\left(ikr\cos(\phi-\psi_2)\sin\theta\right) \\ \vdots \\ \sqrt{g_t(\phi,\theta,\theta_{tilt})} \exp\left(ikr\cos(\phi-\psi_{N_{BS}})\sin\theta\right) \end{bmatrix} \quad (31)
$$

where $\psi_s = \frac{2\pi(s-1)}{N_{BS}}$. With this formulation, the normalized correlation coefficient in the presence of MC between the Tx antenna dipoles s and s' is given by,

$$
\rho_t^{MC}(s,s') = \frac{1}{\sqrt{P_s P_{s'}}} \mathbb{E}[\mathbf{v}_s \mathbf{v}_{s'}^*] \quad (32)
$$

Writing $\mathbf{Z}^{-1}$ as $\mathbf{C}$, and letting $c_{ss'}$ denote the elements of $\mathbf{C}$, $\mathbb{E}[\mathbf{v}_s \mathbf{v}_{s'}^*]$ can be computed as,

$$
\begin{aligned}
\mathbb{E}[\mathbf{v}_s \mathbf{v}_{s'}^*] &= \sum_{m=1}^{N_{BS}} \sum_{n=1}^{N_{BS}} c_{sm} c_{s'n}^* \mathbb{E}[g_t(\phi,\theta,\theta_{tilt}) \exp(ikr \\
&\quad \times \cos(\phi-\psi_m)\sin\theta) \exp\left(-ikr\cos(\phi-\psi_n)\sin\theta\right)], \\
&= \sum_{m=1}^{N_{BS}} \sum_{n=1}^{N_{BS}} c_{sm} c_{s'n}^* \rho_t(m,n), \qquad s,s' = 1,\dots,N_{BS},
\end{aligned} \quad (33)
$$

where $\rho_t(m,n)$ is given by (23). The mean transmitted power P_s, $s = 1,\dots,N_{BS}$ is defined and calculated as,

$$
P_s = \mathbb{E}[|\mathbf{v}_s|^2] \quad (34)
$$

$$
\begin{aligned}
&= \Re[\sum_{m=1}^{N_{BS}} \sum_{n=1}^{N_{BS}} c_{sm} c_{sn}^* \rho_t(m,n)] + \sum_{m=1}^{N_{BS}} |c_{sm}|^2 \rho_t(m,m), \\
&= \sum_{\substack{m=1 \\ m\neq n}}^{N_{BS}} \sum_{n=1}^{N_{BS}} \Re[c_{sm}c_{sn}^*]\Re[\rho_t(m,n)] + \sum_{\substack{m=1 \\ m\neq n}}^{N_{BS}} \sum_{n=1}^{N_{BS}} \Im[c_{sm}c_{sn}^*] \\
&\quad \times \Im[\rho_t(m,n)] + \sum_{m=1}^{N_{BS}} \Re[c_{sm}c_{sm}^*]\rho_t(m,m). \quad (35)
\end{aligned}
$$

Since this derivation is for antenna dipoles, so when using (23) in (33) and (35) the antenna element radiation patterns expressions have to be used, which are the same as (3) and (4), with θ_{3dB} replaced with $\theta_{3dB,E} = 65^o$ [31].

IV. Performance Evaluation of the ULA and UCA configurations

As discussed earlier, accommodating a large number of antennas with sufficient spacing introduces several constraints for practical implementation, given the limited space at the BS and the MS. The problem becomes more acute in massive MIMO settings, where an even larger number of antenna elements needs to be packed in a confined space at the top ot the BS tower. With the advent of FD beamforming techniques that exploit the properties of the elevation domain, the idea of placing the antenna elements in the vertical direction and organizing them into columns or ports is becoming popular and it is interesting to study and compare different configurations for the resulting antenna ports. In this section, we will

compare the performance of the ULA and UCA configurations of antenna ports.

The structure of the UCA was explained in section II-A. The ULA of antenna ports is a popular array configuration proposed in the 3GPP reports on FD-MIMO [17], [26], wherein the antenna elements are arranged in a rectangular array in the $(\hat{\mathbf{e}}_y, \hat{\mathbf{e}}_z)$ plane. The antenna ports are placed at fixed positions along the $\hat{\mathbf{e}}_y$ direction and are numbered in order from 1 to N_{BS}. Each antenna port is mapped to N_E antenna elements arranged along the $\hat{\mathbf{e}}_z$ direction. The topology is shown in Fig. 3. At the receiver side, each antenna port appears as a single antenna, because its elements carry the same signal. We are therefore interested in the channel between the transmitting antenna port and the MS. The SCF for the 3D MIMO channel constituted by the uniform linear array of antenna ports was derived in [28]. This section aims at providing a detailed performance comparison of the two configurations in terms of spatial correlation and MI, under the constraint of equal array widths.

A. Simulation Method and Parameters

The channel parameters in (8) are generated and simulation results are carried out for the 3D urban macro (UMa) and 3D urban micro (UMi) scenarios outlined in the 3GPP and WINNER+ reports [17], [30]. We will consider a point-to-point MIMO system with an outdoor user of height $1.5m$ positioned at the edge of a cell of radius $250m$. The path loss expressions for the non line of sight (NloS) propagation condition of the 3D-UMa and 3D-UMi scenarios are provided in Table 7.2-1 of [17]. The distribution of shadow fading is log-normal, and its standard deviation is also provided in the same table. The BS heights for the 3D-UMa and 3D-UMi scenarios are $25m$ and $10m$ respectively. The values of the mean elevation AoD or the line of sight (LoS) angle for the user, denoted by θ_0, are computed for the two scenarios for the given BS and MS heights and are provided in Table 3. The downtilt angle, θ_{tilt}, is set equal to the elevation LoS angle of the user.

The elevation AoDs/AoAs are generated using the Laplacian elevation angular distribution with parameters θ_0 and σ, where θ_0 is the mean elevation angle and σ is the angular spread in the elevation. The elevation angular spread at the MS, σ_r, is computed using the distribution and parameters specified in Table 7.3-6 of [17] and Table 4-3 of [30]. According to these tables, σ_r is log-normally distributed with mean μ_{ZSA} and spread ϵ_{ZSA} and its mean value is computed to be $10^{1.26} = 18^o$ for the 3D-UMa NLoS and $10^{0.88} = 8^o$ for the 3D-UMi NLoS scenario. The average values for elevation angular spread at the BS, σ_t, for the two scenarios are picked from the WINNER+ calibration results ([30] Table 4-3 p78). All these values are tabulated in Table 3. Some field trials have provided higher values for σ_t for the 3D-UMi scenario, however we carry out the simulations for the calibration results provided in the WINNER+ report [42].

The Von Mises (VM) distribution, with parameters mean azimuth angle μ and azimuth angular spread κ, is used to generate azimuth angles due to its close association with
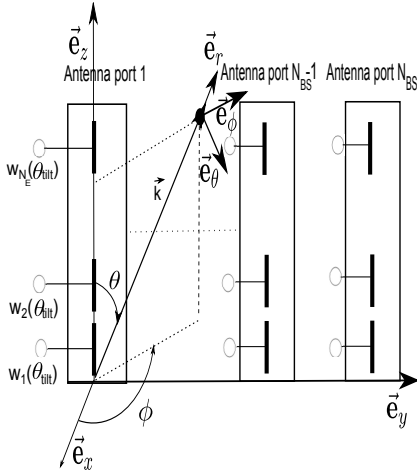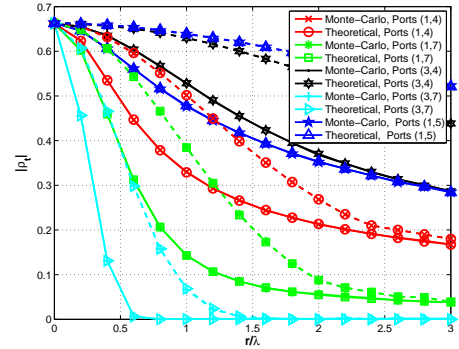
Fig. 3: ULA of antenna ports.

Fig. 4: Correlation between different pairs of Tx antenna ports in the UCA for $\mu = 0$ for the UMa scenario. The dotted lines correspond to $\kappa_t = 30$.

the Wrapped Gaussian (WG) distribution proposed in the standards for the generation of azimuth angles. The values of the azimuth angular spread at the BS and the MS for the WG density, denoted by $\sigma^2_{WG,t}$ and $\sigma^2_{WG,r}$ respectively, are also computed using the parameters specified in Table 7.3-6 of [17]. The values of the corresponding κ_t and κ_r, for the BS and the MS respectively, are obtained using the relationship given in [28] and are provided in Table 3. The comparison for both configurations is done under the same channel conditions with the values of parameters set as tabulated in Table 3, unless stated otherwise in the analysis.

Since the spatial constraints at the BS tower largely determine the choice of the antenna array and the separation between the adjacent ports, so we define the size of the array as its width and keep it equal for both configurations to allow for a fair comparison in terms of the total array size. For the ULA, the normalized width is defined as $(N_{BS} - 1) \times \frac{d_t}{\lambda}$ and for the UCA, it is defined as $2\frac{r}{\lambda}$.

B. Performance in terms of the Spatial Correlation

In this section, we aim to provide a detailed comparison of the spatial correlation experienced by the antenna ports in the UCA and ULA configurations. The spatial correlation coefficients for the Tx and Rx antenna ports for the UCA topology are given in equations (23) and (24) respectively. The expressions for the spatial correlation between the Tx antenna ports and the Rx antenna ports for the ULA configuration were derived in [[28], equations (27) and (28)].

We first validate the result in **Theorem 1** for different pairs of Tx antenna ports for the UCA configuration, by

TABLE III: Simulation parameters for 3D scenarios.

UMa NLoS		UMi NLoS	
Parameter	**Value**	**Parameter**	**Value**
N_{BS}, N_{MS}	8	N_{BS}, N_{MS}	8
θ_0, θ_{tilt}	95.37^o	θ_0, θ_{tilt}	91.95^o
$\sigma^2_{WG,t}, \sigma^2_{WG,r}$	$26^o, 74^o$	$\sigma^2_{WG,t}, \sigma^2_{WG,r}$	$26^o, 69^o$
κ_t, κ_r	6, 2.85	κ_t, κ_r	6, 3
σ_t, σ_r	$8^o, 18^o$	σ_t, σ_r	$4^o, 8^o$
σ_{SF}	6 dB	σ_{SF}	4 dB.

computing the correlation coefficients using the theoretical result in (23) for $N_0 = 18$ summations over n and the Monte-Carlo simulations of (14) over 100000 channel realizations. The correlation values are plotted for the 3D-UMa scenario in Fig. 4 for the antenna port pairs $(1, 4)$, $(1, 7)$, $(3, 4)$, $(3, 7)$ and $(1, 5)$. As expected, the correlation decreases with the increase in the array width and the theoretical result in (23) provides a very good match to the Monte-Carlo simulated correlation using less than twenty summations over n. The correlation values are governed by the interplay between the relative positions of the ports and the values of channel parameters like the mean AoD/AoA and the angular spread. The following discussions and results are organized to study the performance of the two arrays under different parameter sets.

1) Effect of the azimuth spread κ_t and the relative positions of ports in the UCA at $\mu = 0$: For the UCA topology of 8 antenna ports shown in Fig. 2, it is obvious that the correlation values between port 3 and port 4 are the highest among the simulated cases as confirmed in Fig. 4 for the 3D-UMa scenario, due to their adjacent placement and smallest inter-port separation. However, the relative separation between the ports in the pair $(1, 7)$ is also smaller than that between the pair $(1, 4)$, but the correlation values for $(1, 7)$ are lower. This is explained by observing that for the mean azimuth AoD $\mu = 0$, the mean radiation is in $\hat{\mathbf{e}}_x$ direction and the spread is measured along $\hat{\mathbf{e}}_y$ direction. The distance along $\hat{\mathbf{e}}_y$ is shorter for the port pair $(1, 4)$, yielding higher values of correlation for this pair as compared to the values for $(1, 7)$.

Comparing the results for pairs $(1, 5)$ and $(3, 7)$, where the first pair essentially corresponds to two antenna ports placed along the $\hat{\mathbf{e}}_y$ direction and the second pair corresponds to two antenna ports placed along the $\hat{\mathbf{e}}_x$ direction, we observe that the values for $(1, 5)$ are much higher than the values for $(3, 7)$. This is again explained by the fact that for $\mu = 0$, ports 1 and 5 are directly behind each other and in line with the mean AoD, resulting in maximum correlation. Therefore the relative separation of the ports along both $\hat{\mathbf{e}}_x$ and $\hat{\mathbf{e}}_y$ directions together with the mean AoD determines the correlation values.

Increasing κ_t will cause the correlation values for all pairs to increase due to a decrease in the azimuthal spread. This can be seen by observing the dotted lines in Fig. 4, plotted for $\kappa_t = 30$. It is important to note that for $\kappa_t = 30$, the port
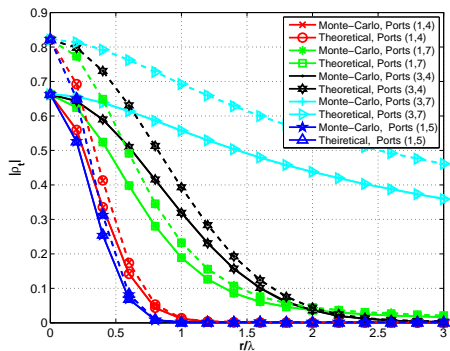
Fig. 5: Correlation between different pairs of Tx antenna ports in the UCA for $\mu = \pi/2$. Solid lines correspond to UMa scenario and dotted lines correspond to UMi scenario.
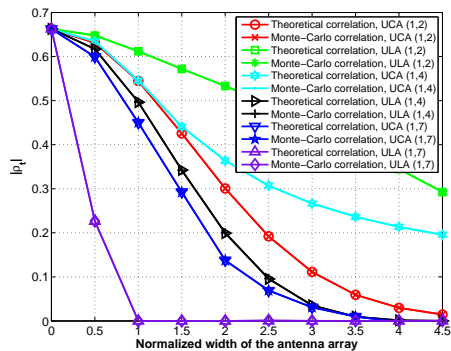

Fig. 6: Comparison of correlation between different Tx antenna port pairs in the UCA and ULA configurations for the 3D-UMa scenario.
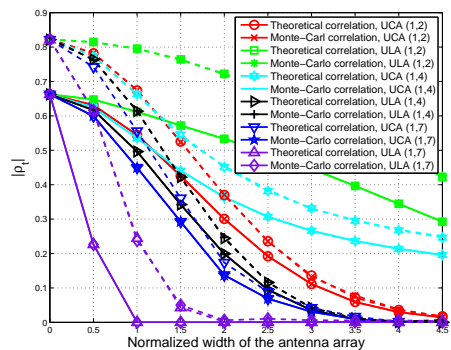

Fig. 7: Comparison of correlation between different Tx antenna port pairs in the UCA and ULA configurations for the 3D-UMa scenario (solid lines) and the 3D-UMi scenario (dotted lines).

pair $(1,5)$ experiences higher correlation than $(3,4)$. Since there is non-zero separation between ports 3 and 4 along the direction of measurement of the azimuthal spread, $\hat{\mathbf{e}}_y$, so for small values of spread this port pair will experience lesser correlation than the pair $(1,5)$ that has zero separation along $\hat{\mathbf{e}}_y$. Even for higher spreads as in the UMa scenario ($\kappa_t = 6$), the gap between the curves for the port pairs $(1,5)$ and $(3,4)$ becomes smaller as r increases, because the separation along the $\hat{\mathbf{e}}_y$ direction for the port pair $(3,4)$ starts to increase.

2) Effect of the elevation angular spread σ_t and relative positions of the ports in the UCA at $\mu = \pi/2$: The correlation values for the Tx antenna port pairs are now plotted for both 3D-UMa (solid lines) and 3D-UMi (dotted lines) scenarios in Fig. 5 for $\mu = \pi/2$. Changing the value of μ to $\pi/2$ yields a different order of results. The correlation in the pair $(1,7)$ is now higher than that in the pair $(1,4)$ because of the shorter relative distance along the direction of the azimuthal spread, which is now measured along the $\hat{\mathbf{e}}_x$ direction. Also the pair $(3,7)$ has the highest correlation because for $\mu = \pi/2$, port 7 is directly behind port 3 and in line with the mean AoD leading to high correlation values. The arrangement of the ports in the $(\hat{\mathbf{e}}_x, \hat{\mathbf{e}}_y)$ plane in a circular fashion, allows μ to impact the order of results. Changes in the mean elevation AoD will only affect the values but not the order of results.

The correlation values for the 3D-UMi scenario are higher for all port pairs. This is because of the lower value of elevation angular spread, σ_t proposed for the UMi scenario in the WINNER+ report. Note that κ_t for both scenarios is the same as tabulated in Table 3. It is interesting to note that although the lower value of σ_t in the 3D-UMi scenario does have the adverse effect of increasing correlation values but it also increases the average Tx power of an antenna port (see the value of $|\rho_t|$ at 0 antenna spacing). This is a consequence of the form of the incorporated vertical antenna pattern in (4).

We now compare the spatial correlation performance of the UCA and the ULA configurations.

3) Effect of the relative positions of ports on the correlation values for the ULA and UCA topologies at $\mu = 0$: The correlation between adjacent Tx antenna ports (i.e. port 1 and port 2) of the UCA configuration is plotted in red in Fig. 6 for the 3D-UMa scenario. We also plot in green on the same figure, the correlation between the adjacent Tx antenna ports (1 and 2) of the ULA configuration. For every value of normalized array width, the correlation between the adjacent antenna ports in the ULA is higher than that experienced by the adjacent ports in the UCA. This is explained by realizing the minimum distance advantage of the UCA topology.

The result for adjacent antenna ports does not hold for all other pairs of ports. The structure of the circular array is different from that of the linear array since the antennas are distributed in the $(\hat{\mathbf{e}}_x, \hat{\mathbf{e}}_y)$ plane in a circular fashion, rather than being placed linearly along one axis. For the ULA, the correlation between port 1 and all subsequent antenna ports will be lower than the correlation between the ports 1 and 2 as shown in Fig. 6. This not true for the UCA, where the values will be greatly influenced by the positions of the ports and the channel parameters as shown in Fig. 4 and Fig. 5. For a fixed width, the separation along $\hat{\mathbf{e}}_y$ (the direction in which the angular spread is measured for $\mu = 0$) between the antenna ports $(1,2)$ is lower in the ULA than that in the UCA, causing the ports to be more correlated in the ULA. However for the second pair, the circular fashion of the arrangement of the antenna ports in the UCA causes the antenna ports 1 and 4 to be closer in the $\hat{\mathbf{e}}_y$ direction and therefore more correlated than they are in the ULA topology. The same conclusion can be drawn for the third pair of antenna ports with a larger gap between the curves, which follows from the higher separation between port 1 and port 7 in the ULA topology.
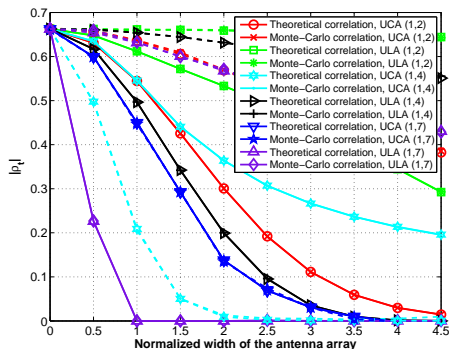
Fig. 8: Comparison of correlation for $\mu = 0$ (solid lines) and $\mu = \pi/2$ (dotted lines) in the 3D-UMa scenario.
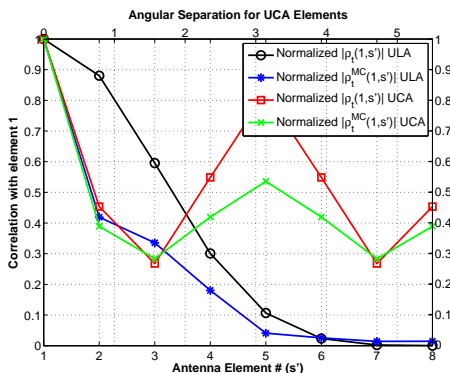

Fig. 9: Comparison of correlation in the ULA and UCA topologies with and without accounting for MC in the UMa scenario.

4) Effect of the angular spreads on the relative correlation values for ULA and UCA: The performance of both ULA and the UCA is angular spread dependent as can be seen in Fig. 7 plotted for the 3D-UMa scenario (solid lines) and the 3D-UMi scenario (dotted lines), where the latter has a smaller elevation angular spread [30]. It is interesting to see that ULA is more sensitive to changes in the spread, with the correlation decreasing more rapidly in the 3D UMa scenario, which has a higher elevation spread, as compared to the decrease for the UCA. This result implies the ULA can perform better in rich scattering environments where the angular spread is generally high. Note that the Tx power of each antenna port is higher in the UMi case; a consequence of the incorporation of the vertical antenna radiation pattern with a small $3\mathrm{dB}$ beamwidth in (4) into the channel model.

5) Effect of the mean azimuth AoD on the correlation values for ULA and UCA: We plot the correlation coefficients for $\mu = 0$ (solid lines) and $\mu = \pi/2$ (dotted lines) in Fig. 8 for the 3D-UMa scenario. The performance of the ULA deteriorates a lot for $\mu = \pi/2$, which corresponds to the endfire region of the ULA. This is due to the fact that all the ports are placed in the direction of the mean AoD. The correlation values for the ports in the UCA will depend on the relative position of the pair of ports under study as discussed in Fig. 5.

6) Effect of mutual coupling on the performance of the ULA and the UCA configurations: In this section, we focus on 8 antenna elements arranged in the ULA and UCA topologies and plot in Fig. 9 the normalized correlation coefficients

with and without accounting for the MC effects in the 3D-UMa scenario. The expression for $|\rho_t^{MC}|$ in (32) is already normalized by the average antenna powers P_s and $P_{s'}$. The normalized correlation values without accounting for the MC effects, $|\rho_t|$, can be computed using (23), normalized with the average antenna gains to allow for a fair comparison. The curves for the ULA topology for both cases are obtained using expressions from [28]. The coefficients are plotted for all antenna elements with reference to antenna element 1 for the normalized array width of 3λ. An additional axis is provided on the top of the figure for the UCA, representing the angular separation of each element with the reference element 1.

The results in Fig. 9 show that the MC can, contrary to common belief, actually decrease the spatial correlation level between the channel coefficients, especially for antennas placed close to each other in the direction of the angular spread $\hat{\mathbf{e}}_y$. This favorable result is explained by the fact that the MC effect causes antenna pattern distortion and provides some form of pattern diversity [18], [40]. In compact MIMO arrays, this pattern diversity effect dominates over the effect of the loss in spatial diversity. This has been observed in [18], [20], [38], wherein the authors reason that the coupling phenomenon actually decorrelates the signals by acting as an additional "channel". In short, the advantage we lose from decreased antenna separation is more than compensated when we take the MC effects into account.

However, this figure did not study the impact of MC on the antenna gain and average Tx power. For this purpose, we plot in Fig. 10 the results for both topologies without normalizing the correlation with P_s and $P_{s'}$. The value of $|\rho_t|$ at $s' = 1$ is essentially $\rho_t(1,1)$, which represents the average transmitted power by an individual antenna. The result reveals that while MC decorrelates the channel coefficients, it also introduces a significant power loss [39], [40]. Moreover, Fig. 10 shows that ULA is more sensitive to the MC effects.

To conclude, there is a strong interplay between the channel and array parameters in determining the spatial correlation experienced by the two arrays under study. Even though the correlation experienced by the adjacent pair of antenna ports is lower in the UCA, but this can not be the only metric to dictate the choice of the antenna topology for different propagation scenarios. The ULA configuration might achieve a lower overall correlation under some channel conditions. We will resort to the MI analysis to see the overall effect of the spatial correlation and draw some conclusions on the performance of the two arrays in the 3D-UMa and 3D-UMi scenarios.

C. Mutual Information Performance Comparison in a Point-to-Point MIMO System

In this section, we compare the MI performance of the two arrays under discussion to draw some important conclusions on the efficiency of these compact arrays in a correlated environment. For this purpose, we use the Kronecker channel model, which is suitable for the information-theoretic analysis of the MI and is defined as [1],

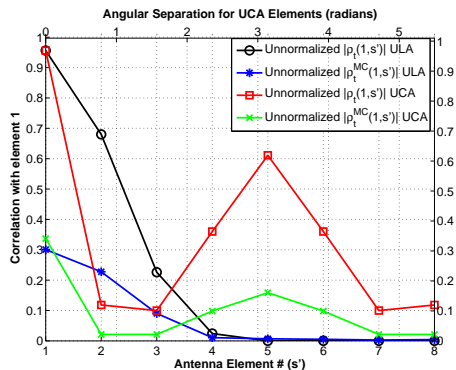$$\mathbf{H} = \mathbf{R}_{MS}^{\frac{1}{2}} \mathbf{X} \mathbf{R}_{BS}^{\frac{1}{2}}, \tag{36}$$

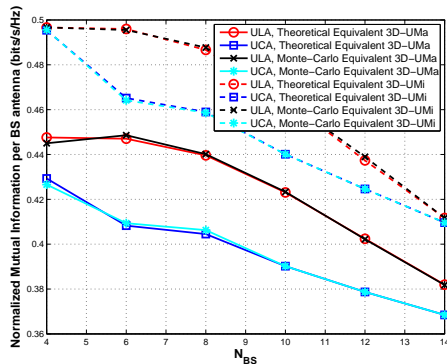Fig. 10: Comparison of unnormalized correlation in the ULA and UCA topologies with and without accounting for MC.

Fig. 11: Comparison of MI for the UCA and ULA configurations for array width=6λ.

where $\mathbf{X}$ is a N_{MS}xN_{BS} matrix whose entries are i.i.d $\mathcal{CN}(0,1)$, $\mathbf{R}_{MS}$ is the correlation matrix at the MS and $\mathbf{R}_{BS}$ is the correlation matrix at the BS. For the UCA configuration, $[\mathbf{R}_{MS}]_{u,u'} = \rho_r(u,u')$ and $[\mathbf{R}_{BS}]_{s,s'} = \rho_t(s,s')$, where $\rho_t(s,s')$, $\rho_r(u,u')$ are given by equations (23) and (24) respectively. For the ULA, $[\mathbf{R}_{MS}]_{u,u'} = \rho_r(u-u')$, $[\mathbf{R}_{BS}]_{s,s'} = \rho_t(s-s')$, where $\rho_t(s-s')$, $\rho_r(u-u')$ are obtained using the derived expressions in [28].

The downlink of a single cell with a point-to-point MIMO system is considered in this section with the channel parameters tabulated in Table 3. The MI of the N_{MS}xN_{BS} MIMO system with equal power-allocation is given by,

$$I(SNR) = \log \det \left(\mathbf{I}_{N_{MS}} + (SNR/N_{BS})\mathbf{H}\mathbf{H}^H \right), \quad (37)$$

where $\mathbf{H}$ is the N_{MS}xN_{BS} channel matrix in (36) and SNR is the received signal-to-noise ratio.

A closed-form expression for the distribution of the MI for the Kronecker model is difficult to derive. Fortunately, tools from RMT provide us with some simple deterministic equivalents of the distribution of the MI in the large (N_{BS}, N_{MS}) regime. These approximations are accurate for moderate system sizes as well. This paper uses the deterministic equivalent provided in Theorem 1 in [29] which says that under assumptions **A1** and **A2** in [29] on the correlation matrices, the ergodic MI of the Kronecker channel converges almost surely to a deterministic term, i.e.,

$$\frac{1}{N_{BS}}\mathbb{E}[I(SNR)] - V(SNR) \xrightarrow[N_{BS},N_{MS}\to\infty]{a.s} 0, \quad (38)$$

where the expression for $V(SNR)$ is provided in Theorem 1 in [29].

This result is used to compare the MI achieved by the two configurations in the 3D-UMa and 3D-UMi scenarios. The correlation coefficients are computed for N_{BS} and N_{MS} ranging from 4 to 14 and are used to form the matrices $\mathbf{R}_{BS}$ and $\mathbf{R}_{MS}$. Monte-Carlo simulations of (37) are performed over 3000 channel realizations of (36) to obtain the simulated MI that is plotted along with the theoretical MI obtained using the deterministic equivalent $V(SNR)$ in the subsequent figures.

1) Effect of relative positioning of ports and angular spreads: As discussed in the last subsection, even though the correlation between the adjacent antenna ports in the UCA is lower than that in the ULA, the ULA can still achieve a lower overall correlation. The circular fashion of arrangement of the antenna ports in the UCA causes correlation of the ports with a reference port to first decrease and then increase as we traverse the array while the correlation of all subsequent ports in the ULA decreases as we move from port 1 to N_{BS}. In particular for higher angular spreads as in the 3D-UMa scenario, with the AoDs/AoAs concentrated near the broadside of the array, i.e. for $\mu = 0$, the overall correlation in the channel constituted by the ULA decreases faster as shown in Fig. 7. Consequently, the ULA configuration achieves higher values of MI as shown in Fig. 11 plotted for normalized array width of 6λ. Moreover, the theoretical result in (38) coincides well with the the Monte-Carlo simulated MI for the Kronecker channel model for a moderate number of antennas.

Another important insight to be drawn from this result is that even through the correlation values for all port pairs are higher in the 3D-UMi scenario because of the lower elevation spread as shown in Fig. 7, which is disadvantageous but at the same time for the user within the direction of the antenna boresight, i.e. having $\theta_0 = \theta_{tilt}$, the form of vertical antenna pattern with a narrow 3dB beamwidth, is such that the Tx power increases with the decrease in elevation spread (observe the values of ρ_t at $r/\lambda = 0$ in Fig. 5 and 7). This is because the energy of a higher number of propagation paths is captured by the Tx antenna pattern for scenarios with small elevation spreads. As a consequence, the MI values for the 3D-UMi scenario for both array configurations are higher than the values for the 3D-UMa case as shown in Fig. 11 because the effect of the increase in the transmitted power dominates over the adverse effect of increase in correlation.

2) Effect of inter-port spacing: As the number of antenna ports packed in the same width increases, the ports will become very closely positioned in the linear array. The circular fashion of arrangement of antenna ports in the UCA will allow for a relatively higher separation between the ports. The adverse effect of the smaller inter-port separation in the ULA dominates over the adverse effect of the eventual increase in the values of correlation of the subsequent ports with the reference port as we move around the UCA configuration, which results in a higher overall correlation in the MIMO channel
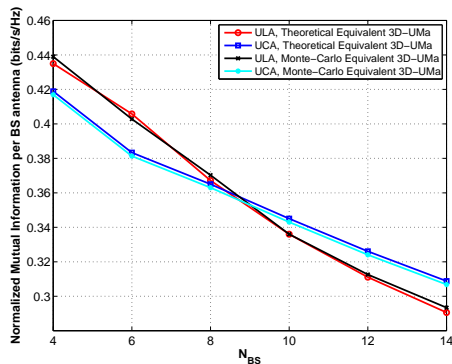
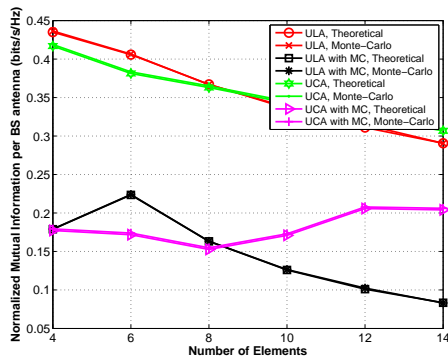Fig. 12: Comparison of MI for the UCA and ULA configurations for width=3λ in the 3D-UMa scenario.

Fig. 13: Comparison of MI for the UCA and ULA configurations with and without accounting for the MC effects for width=3λ.

constituted by ULAs. Therefore, the UCA outperforms the ULA as the ratio of the number of antenna ports to the array width increases. We observe this by plotting the MI for the normalized width = 3λ in Fig. 12 for the 3D-UMa scenario, and see that in this case for $N_{BS} > 8$, the ULA topology achieves a lower MI. The choice of antenna topology for a deployment scenario is therefore largely governed by the ratio of the number of antennas to the width of the array. This result is extremely important in the context of massive MIMO systems, where a large number of antennas have to be packed in a small spatial area. Here the UCA will outperform the ULA topology and can prove to be a more effective choice for capacity maximization.

3) Effect of mutual coupling: As discussed in the last subsection, the effect of mutual coupling is twofold. Firstly it reduces the correlation between the antennas elements as seen in Fig. 9, which is a desirable effect. On the other hand, it introduces an extra power loss as seen in Fig. 10, which is an undesirable effect. Now we will study the combination of these two effects on the MI of the MIMO systems constituted by the ULA and UCA topologies. The result is plotted in Fig. 13 for normalized array width of 3λ for the 3D-UMa scenario. From the result, it is obvious that MC adds extra degradation to the MI for both topologies because the adverse effect of the decrease in the transmitted power dominates over the positive effect of the decrease in correlation. Also, the deterioration is worse for the ULA topology since it is more sensitive to the MC effects. For high values of number of

elements to array width ratio, the UCA outperforms the ULA as discussed in the last result. Also, the increase in the MI values for the UCA with MC case (see pink curves) when 'Number of elements' increases from 8 to 10 is explained by the fact that as the inter-port separation decreases, the pattern diversity and hence the decorrelation effect becomes very dominant, resulting in an improvement in performance. However, the overall performance when accounting for MC effects is definitely worse because of the power loss.

All in all, the performance of antenna arrays depends on several factors including the channel parameters parametrized by the angular spread and the mean AoD/AoA and the array parameters like the number of antennas and the array width. Results show that for similar array sizes, the ULA outperforms the UCA for high angular spreads and low number of antennas to array width ratio, making it a suitable candidate in rich scattering environments, such as the proposed 3D-UMa scenario in WINNER+. However, UCA is a more appropriate choice in massive MIMO systems, where a large number of antennas needs to be deployed in a confined space so as to minimize the overall correlation while reaping the benefits of MIMO techniques. To the best of the authors' knowledge, these useful results have not been observed by a research paper before.

V. CONCLUSION

We proposed a generalized analytical expression for the SCF for the FD-MIMO channel constituted by UCAs of antenna ports at the BS and the MS. The two ingredients of the analysis are the SHE of plane waves and the trigonometric expansion of Legendre polynomials. The novelty of the proposed method lies in the SCF being valid for any propagation environment. The spatial correlation expressions accounting for the MC effects are also derived. Using these results, we compared the correlation and MI performance of two antenna array topologies proposed for FD-MIMO implementation, the ULA and the UCA of antenna ports, by utilizing the information-theoretic deterministic equivalent of the MI developed for the Kronecker channel model. The performance patterns of the two arrays are investigated as a function of the mean AoD/AoA, angular spreads, number of antennas and antenna spacing. It must be emphasized that both the azimuth and elevation parameters must be taken into account so that an accurate performance comparison can be made. Results show that for similar array sizes, the ULA outperforms the UCA for high angular spreads and low number of antennas to array width ratio, making it a suitable candidate for rich scattering environments. However, UCA is a more appropriate choice in massive MIMO settings. Also, ULA is more prone to the power loss introduced by MC between the antenna elements. The conclusions drawn will assist researchers and industrials in the selection of the best antenna array topology for deployment in the emerging FD-MIMO settings.

APPENDIX A
MATHEMATICAL PRELIMINARIES

A. Spherical Harmonics

Spherical harmonics, $Y_n^m(\phi, \theta)$, provide orthonormal basis functions for the representation of functions on the 2-sphere

and are defined for integer degree $n \geq 0$ and integer order $|m| \leq n$ as,

$$Y_n^m(\hat{\mathbf{x}}) = Y_n^m(\phi, \theta) = N_n^m P_n^m(\cos\theta)\exp(im\phi), \quad (39)$$

where $N_n^m = \sqrt{\frac{2n+1(n-m)!}{4\pi(n+m)!}}$.

The array response of an antenna port can be expressed as a superposition of spherical waves, by exploiting the SHE result for a plane electromagnetic wave given by [43],

$$e^{ik\hat{\mathbf{v}}\cdot\mathbf{x}} = \sum_{n=0}^{\infty} i^n(2n+1)j_n(k||\mathbf{x}||)P_n(\hat{\mathbf{v}}\cdot\hat{\mathbf{x}}), \mathbf{x}\in\mathbb{R}^3, \quad (40)$$

where i is the imaginary unit, k is the wave number, $\mathbf{x}$ is the position vector in $\mathbb{R}^3$, $\hat{\mathbf{x}}$ is the corresponding unit vector, $\hat{\mathbf{v}}$ is the unit vector in the direction of wave propagation, j_n is the spherical Bessel function of order n and P_n is the Legendre polynomial function of order n. Let (ϕ_1, θ_1) and (ϕ_2, θ_2) be the spherical coordinates of the vectors $\hat{\mathbf{v}}$ and $\hat{\mathbf{x}}$ respectively, then by the Legendre addition theorem [43],

$$P_n(\hat{\mathbf{v}}\cdot\hat{\mathbf{x}}) = \frac{4\pi}{2n+1}\sum_{m=-n}^{m=n} Y_n^m(\hat{\mathbf{v}})Y_n^{m*}(\hat{\mathbf{x}}),$$

$$= P_n(\cos\theta_1)P_n(\cos\theta_2) + 2\sum_{m=1}^{n}\frac{(n-m)!}{(n+m)!}P_n^m(\cos\theta_1)$$

$$\times P_n^m(\cos\theta_2)\cos[m(\phi_1-\phi_2)], \quad (41)$$

where P_n^m are the associated Legendre polynomials.

B. Properties of Legendre Polynomials

The following properties of Legendre polynomials will be exploited in our analysis.

$$P_n(0) = 0 \text{ for odd } n, P_n^m(0) = 0 \text{ for odd } n+m, \text{ and}$$
$$P_0(x) = 1. \quad (42)$$

Also the Legendre and associated Legendre polynomials can be expanded as [44],

$$P_{2n}(\cos x) = p_n^2 + 2\sum_{k=1}^{n} p_{n-k}p_{n+k}\cos(2kx),$$

$$\bar{P}_{2n}^{2m}(\cos x) = \sum_{k=0}^{n} c_{2n,2k}^{2m}\cos(2kx), \quad (43)$$

$$\bar{P}_{2n-1}^{2m-1}(\cos x) = \sum_{k=1}^{n} d_{2n-1,2k-1}^{2m-1}\sin((2k-1)x),$$

where the coefficients p_n, $c_{2n,2k}^{2m}$ and $d_{2n-1,2k-1}^{2m-1}$ are generated using the recursion relations in [44].

APPENDIX B
PROOF OF THEOREM 1

The expectation terms in (21) can be expressed as a linear combination of the FS coefficients of the power spectra. For the azimuth angles, we have $p_\phi(\phi) = f_\phi(\phi)$, and therefore,

$$\mathbb{E}[\cos(2m\phi)g_{t,H}(\phi)] = \int_{-\pi}^{\pi}\cos(2m\phi)g_{t,H}(\phi)f_\phi(\phi)d\phi$$

$$= \int_{-\pi}^{\pi}\cos(2m\phi)\text{PAS}_t(\phi)d\phi.$$

$$\mathbb{E}[\sin(2m\phi)g_{t,H}(\phi)] = \int_{-\pi}^{\pi}\sin(2m\phi)g_{t,H}(\phi)f_\phi(\phi)d\phi$$

$$= \int_{-\pi}^{\pi}\sin(2m\phi)\text{PAS}_t(\phi)d\phi.$$

$$\mathbb{E}[\cos((2m-1)\phi)g_{t,H}(\phi)] = \int_{-\pi}^{\pi}\cos((2m-1)\phi)g_{t,H}(\phi)f_\phi(\phi)d\phi$$

$$= \int_{-\pi}^{\pi}\cos((2m-1)\phi)\text{PAS}_t(\phi)d\phi.$$

$$\mathbb{E}[\sin((2m-1)\phi)g_{t,H}(\phi)] = \int_{-\pi}^{\pi}\sin((2m-1)\phi)g_{t,H}(\phi)f_\phi(\phi)d\phi$$

$$= \int_{-\pi}^{\pi}\sin((2m-1)\phi)\text{PAS}_t(\phi)d\phi.$$

For the expectation terms involving the elevation angles, we exploit the results on Legendre polynomial expansion in (43) [44] and the relationship in (10) to expand them as,

$$\mathbb{E}[P_{2n}(\cos\theta)g_{t,V}(\theta,\theta_{tilt})] = \sum_{k=-n}^{n}\left[p_{n-k}p_{n+k}\int_0^{2\pi}\cos(2k\theta)\right.$$

$$\left.\times g_{t,V}(\theta,\theta_{tilt})p_\theta(\theta)\sin(\theta)d\theta\right],$$

$$= \sum_{k=-n}^{n} p_{n-k}p_{n+k}\left[\frac{1}{2}\int_0^{2\pi}\sin((2k+1)\theta)\text{PES}_t(\theta,\theta_{tilt})d\theta\right.$$

$$\left.-\frac{1}{2}\int_0^{2\pi}\sin((2k-1)\theta)\text{PES}_t(\theta,\theta_{tilt})d\theta\right].$$

$$\mathbb{E}[\bar{P}_{2n}^{2m}(\cos(\theta))g_{t,V}(\theta,\theta_{tilt})] = \sum_{k=0}^{n}\left[c_{2n,2k}^{2m}\int_0^{2\pi}\cos(2k\theta)\right.$$

$$\left.\times g_{t,V}(\theta,\theta_{tilt})p_\theta(\theta)\sin(\theta)d\theta\right],$$

$$= \sum_{k=0}^{n} c_{2n,2k}^{2m}\left[\frac{1}{2}\int_0^{2\pi}\sin((2k+1)\theta)\text{PES}_t(\theta,\theta_{tilt})d\theta\right.$$

$$\left.-\frac{1}{2}\int_0^{2\pi}\sin((2k-1)\theta)\text{PES}_t(\theta,\theta_{tilt})d\theta\right].$$

$$\mathbb{E}[\bar{P}_{2n-1}^{2m-1}(\cos(\theta))g_{t,V}(\theta,\theta_{tilt})] = \sum_{k=1}^{n}\left[d_{2n-1,2k-1}^{2m-1}\right.$$

$$\left.\times\int_0^{2\pi}\sin((2k-1)\theta)g_{t,V}(\theta,\theta_{tilt})p_\theta(\theta)\sin(\theta)d\theta\right],$$

$$= \sum_{k=1}^{n} d_{2n-1,2k-1}^{2m-1}\left[\frac{1}{2}\int_0^{2\pi}\cos((2k-2)\theta)\text{PES}_t(\theta,\theta_{tilt})d\theta\right.$$

$$\left.-\frac{1}{2}\int_0^{2\pi}\cos((2k)\theta)\text{PES}_t(\theta,\theta_{tilt})d\theta\right].$$

Using the definitions of the FS coefficients given in (25)-(28), we can express the expectation terms involving the azimuth and the elevation angles as a linear combination of the scaled FS coefficients of the PAS and PES. Plugging the resulting expressions in (21) will yield an analytical expression for $\rho_t(s, s')$. This completes the proof of **Theorem 1**.

REFERENCES

[1] D.-S. Shiu, G. J. Foschini, M. J. Gans, and J. M. Kahn, "Fading correlation and its effect on the capacity of multielement antenna systems," *IEEE Transactions on Communications*, vol. 48, no. 3, pp. 502–513, 2000.

[2] C.-N. Chuah, D. N. C. Tse, J. M. Kahn, and R. A. Valenzuela, "Capacity scaling in MIMO wireless systems under correlated fading," *IEEE Transactions on Information Theory*, vol. 48, no. 3, pp. 637–650, 2002.

[3] J. Kermoal, L. Schumacher, P. Mogensen, and K. Pedersen, "Experimental investigation of correlation properties of MIMO radio channels for indoor picocell scenarios," in *IEEE Vehicular Technology Conference (VTC)*, vol. 1, 2000, pp. 14–21.

[4] E. Dahlman, S. Parkvall, J. Sköld, and P. Beming, *3G Evolution, Second Edition: HSPA and LTE for Mobile Broadband*, 2nd ed. Academic Press, 2008.

[5] A. Forenza, D. J. Love, and R. W. Heath, "Simplified spatial correlation models for clustered MIMO channels with different array configurations," *IEEE Transactions on Vehicular Technology*, vol. 56, no. 4, pp. 1924–1934, July 2007.

[6] W. J. L. Queiroz, F. Madeiro, W. T. A. Lopes, and M. S. Alencar, "Spatial correlation for DoA characterization using Von Mises, Cosine, and Gaussian distributions," *International Journal of Antennas and Propagation*, vol. 2011, July 2011.

[7] J. Salz and J. Winters, "Effect of fading correlation on adaptive arrays in digital mobile radio," *IEEE Transactions on Vehicular Technology*, vol. 43, no. 4, pp. 1049–1057, Nov 1994.

[8] J. Zhou, S. Sasaki, S. Muramatsu, H. Kikuchi, and Y. Onozato, "Spatial correlation for a circular antenna array and its applications in wireless communication," in *IEEE Global Telecommunications Conference, GLOBECOM*, vol. 2, Dec. 2003, pp. 1108–1113.

[9] Y. Song, X. Yun, S. Nagata, and L. Chen, "Investigation on elevation beamforming for future LTE-Advanced," in *IEEE International Conference on Communications Workshops (ICC)*, June 2013, pp. 106–110.

[10] J. Koppenborg, H. Halbauer, S. Saur, and C. Hoek, "3D beamforming trials with an active antenna array," in *ITG Workshop on Smart Antennas*, 2012, pp. 110–114.

[11] L. Thiele, T. Wirth, K. Börner, M. Olbrich, V. Jungnickel, J. Rumold, and S. Fritze, "Modeling of 3D field patterns of downtilted antennas and their impact on cellular systems," in *ITG Workshop on Smart Antennas,*, 2009.

[12] Y. H. Nam, B. L. Ng, K. Sayana, Y. Li, J. Zhang, Y. Kim, and J. Lee, "Full-dimension MIMO (FD-MIMO) for next generation cellular technology," *IEEE Communications Magazine*, vol. 51, no. 6, pp. 172–179, June 2013.

[13] Y. Kim, H. Ji, J. Lee, Y. H. Nam, B. L. Ng, I. Tzanidis, Y. Li, and J. Zhang, "Full dimension MIMO (FD-MIMO): the next evolution of MIMO in LTE systems," *IEEE Wireless Communications*, vol. 21, no. 2, pp. 26–33, April 2014.

[14] R1-122034, "Study on 3D channel Model for elevation beamforming and FD-MIMO studies for LTE," 3GPP TSG RAN Plenary no. 58, Barcelona, Spain, Dec. 2012.

[15] 3GPP TR 36.897 V13.0.0 , "Study on elevation beamforming/Full-Dimension (FD) MIMO for LTE ," June 2015.

[16] W. Zhang, J. Xiang *et al.*, "Field trial and future enhancements for TDD massive MIMO networks," in *IEEE 26th International Symposium on Personal, Indoor, and Mobile Radio Communications (PIMRC)*, Aug. 2015, pp. 2339–2343.

[17] 3GPP TR 36.873 V12.0.0, "Study on 3D channel model for LTE," Sep. 2014.

[18] J. Luo, J. R. Zeidler, and S. McLaughlin, "Performance analysis of compact antenna arrays with MRC in correlated nakagami fading channels," *IEEE Transactions on Vehicular Technology*, vol. 50, no. 1, pp. 267–277, Jan. 2001.

[19] S. K. Yong and J. Thompson, "Three-dimensional spatial fading correlation models for compact MIMO receivers," *IEEE Transactions on Wireless Communications*, vol. 4, no. 6, pp. 2856–2869, Nov. 2005.

[20] J. Zhou, J. Chen, L. Qiu, and H. Kikuchi, "Effects of antenna correlation and mutual coupling on the performance of MIMO system in a three-dimensional multipath channel," in *Global Symposium on Millimeter Waves (GSMM)*, May 2012, pp. 139–142.

[21] P. D. Teal, T. D. Abhayapala, and R. A. Kennedy, "Spatial correlation for general distributions of scatterers," *IEEE Signal Processing Letters*, vol. 9, no. 10, pp. 305–308, Oct. 2002.

[22] K. Mammasis, R. Stewart, and J. Thompson, "Spatial fading correlation model using mixtures of von mises fisher distributions," *IEEE Transactions on Wireless Communications*, vol. 8, no. 4, pp. 2046–2055, April 2009.

[23] H. Rogier, "Spatial correlation in uniform circular arrays based on a spherical-waves model for mutual coupling," *AEUE - International Journal of Electronics and Communications*, vol. 60, no. 7, pp. 521–532, 2006.

[24] K. Mammasis and R. W. Stewart, "Spherical statistics and spatial correlation for multielement antenna systems," *EURASIP Journal on Wireless Communications and Networking*, vol. 2010, Dec. 2010.

[25] M. Shafi, M. Zhang, A. L. Moustakas, P. J. Smith, A. F. Molisch, F. Tufvesson, and S. H. Simon, "Polarized MIMO channels in 3D: Models, measurements and mutual information," *IEEE Journal on Selected Areas in Communications*, vol. 24, no. 3, pp. 514–527, 2006.

[26] 3GPP TR 37.840 V12.00, "Study of radio frequency (RF) and electromagnetic compatibility (EMC) requirements for active antenna array system (AAS) base station," Mar. 2013.

[27] J.-A. Tsai, R. Buehrer, and B. Woerner, "BER performance of a uniform circular array versus a uniform linear array in a mobile radio environment," *IEEE Transactions on Wireless Communications,*, vol. 3, no. 3, pp. 695–700, May 2004.

[28] Q.-U.-A. Nadeem, A. Kammoun, M. Debbah, and M.-S. Alouini, "A generalized spatial correlation model for 3D MIMO channels based on the fourier coefficients of power spectrums," *IEEE Transactions on Signal Processing*, vol. 63, no. 14, pp. 3671–3686, July 2015.

[29] W. Hachem, O. Khorunzhiy, P. Loubaton, J. Najim, and L. Pastur, "A new approach for mutual information analysis of large dimensional multi-antenna channels," *IEEE Transactions on Information Theory*, vol. 54, no. 9, pp. 3987–4004, 2008.

[30] J. Meinilä, P. Kyösti *et al.*, "D5.3: WINNER+ Final Channel Models V1.0," [Online.] Available: http://projects.celtic-initiative.org/winner+ /WINNER+%20Deliverables/D5.3_v1.0.pdf, June. 2010.

[31] A. Kammoun, H. Khanfir, Z. Altman, M. Debbah, and M. Kamoun, "Preliminary results on 3D channel modeling: From theory to standardization," *IEEE Journal on Selected Areas in Communications*, vol. 32, no. 6, pp. 1219–1229, June. 2014.

[32] C. A. Balanis, *Antenna theory analysis and design*. New Jersey, USA: John Wiley & Sons, Inc., 2005.

[33] Radiocommunication Sector of International Telecommunication Union, "Report ITU-R M.2135-1: Guidelines for evaluation of radio interface technologies for IMT-advanced," 2009.

[34] 3GPP TR 36.814 V9.0.0 , "Further advancements for E-UTRA physical layer aspects (Release 9)," March 2010.

[35] K. Pedersen, P. Mogensen, and B. Fleury, "Spatial channel characteristics in outdoor environments and their impact on bs antenna system performance," in *IEEE Vehicular Technology Conference*, vol. 2, 1998, pp. 719–723 vol.2.

[36] K. Kalliola, K. Sulonen, H. Laitinen, O. Kivekas, J. Krogerus, and P. Vainikainen, "Angular power distribution and mean effective gain of mobile antenna in different propagation environments," *IEEE Transactions on Vehicular Technology*, vol. 51, no. 5, pp. 823–838, Sep. 2002.

[37] T. Abhayapala, T. Pollock, and R. Kennedy, "Characterization of 3D spatial wireless channels," in *IEEE Vehicular Technology Conference (VTC 2003-Fall)*, vol. 1, Oct. 2003, pp. 123–127.

[38] T. Svantesson and A. Ranheim, "Mutual coupling effects on the capacity of multielement antenna systems," in *IEEE International Conference on Acoustics, Speech, and Signal Processing*, vol. 4, 2001, pp. 2485–2488.

[39] Y. Wu, J. Linnartz, J. Bergmans, and S. Attallah, "Effects of antenna mutual coupling on the performance of MIMO systems," in *29th Symposium on Information Theory*, May 2008.

[40] B. Clerckx, D. Vanhoenacker-Janvier, C. Oestges, and L. Vandendorpe, "Mutual coupling effects on the channel capacity and the space-time processing of MIMO communication systems," in *IEEE International Conference on Communications (ICC)*, vol. 4, May 2003, pp. 2638–2642 vol.4.

[41] G. J. Foschini and M. J. Gans, "On limits of wireless communications in a fading environment when using multiple antennas," *Wireless Personal Communications.*, vol. 6, no. 3, pp. 311–335, Mar. 1998. [Online]. Available: http://dx.doi.org/10.1023/A:1008889222784

[42] J. Zhang, C. Pan, F. Pei, G. Liu, and X. Cheng, "Three-dimensional fading channel models: A survey of elevation angle research," *IEEE Communications Magazine*, vol. 52, no. 6, pp. 218–226, June 2014.

[43] D. Colton and R. Kress, *Inverse Acoustic and Electromagnetic Scattering Theory*, 3rd ed. New York, NY: Springer, 2013.

[44] D. J. Hofsommer and M. L. Potters, "Table of fourier coefficients of associated legendre functions," R 478 Computation Department of the Mathematical Center, Amsterdam, June 1960.